Journal of Imaging Science and Technology® 50(3): 217–227, 2006.

Feature Article: Omnidirectional Scene Illuminant Estimation Using A Mirrored Ball

Shoji Tominaga and Norihiro Tanaka[†]
Department of Engineering Informatics, Osaka Electro-Communication University, Neyagawa, Osaka 572-8530, Japan
E-mail: shoji@tmlab.osakac.ac.jp

Abstract. *This paper proposes a method for estimating the omnidirectional distribution of the scene illuminant spectrum from images taken by a camera aimed at a mirrored ball. First, we introduce measuring systems using a RGB color camera and a mirrored ball placed at an arbitrary location in a natural scene for acquiring ambient light from any direction. Second, in order to estimate the direction from which light comes to the ball, we calibrate the measuring systems and determine a mapping between the image coordinates of the spherical ball and the directions of light rays in the world. An omnidirectional image representing the spatial distribution of ambient light sources is created in a polar coordinate system. Third, we present an algorithm for recovering the illuminant spectral power distribution from the image data at each pixel and the reflectance data of the mirrored ball. Finally, we execute an experiment in a natural environment with multiple light sources for examining the feasibility of the proposed method. © 2006 Society for Imaging Science and Technology.*
[DOI: 10.2352/J.ImagingSci.Technol.(2006)50:3(217)]

INTRODUCTION

The problem of scene illuminant estimation from image data has a long history, and the estimation algorithms have applications in many fields of color science, computer vision, image processing, image reproduction, and image database retrieval.[1] So far, most of the estimation methods assumed a single illumination source.

However, we should note that many illumination sources are present in natural scenes. The case of just one source is an exception. For example, an indoor scene may have electric light sources of ceiling lamps, table lamps, and natural light sources shining through windows. An outdoor scene may have the direct illumination source of the sunlight and the second source of the sky. Hubel[2] made an interesting observation about the perception of object color lit by sunlight at dawn and dusk. When the sunlight illuminates objects or persons, the surfaces impart a characteristic warm glow. An indoor scene illuminated by a tungsten light of color temperature and spectral distribution identical to sunlight does not cause any similar perception. The visual system can distinguish the scene lit by dawn and dusk light from the scene lit by the tungsten light. He explained that the color gamut observed in the outdoor scene is much larger than the gamut under a single illumination source. The main objects in the scene are illuminated by the direct sunlight and the shadows are illuminated by the second source of the blue sky.

Therefore, illuminant estimation in natural scenes includes the problem of estimating a spatial distribution of light sources by omnidirectional observations. Previous omnidirectional measuring systems used a mirrored ball,[3–6] a fisheye lens,[7,8] and a hyperbolic or parabolic mirror.[9,10] These measuring systems were mostly developed for computer graphics and computer vision. A mirrored ball is convenient to observe the surrounding scene of the ball placed at a particular point in space, because a mirrored ball and a camera are independent. The other measuring systems incorporate a fisheye lens or a reflecting mirror into conventional camera systems. The observable range of a mirrored ball is much wider than the range of the other systems. Debevec[4] is a pioneer in the development of a technique using a mirrored ball in computer graphics, called a light probe. He was successful in creating images of synthetic objects in real scenes.[11] Unger et al.[5] proposed an array of mirrored spheres to capture the spatially varying illumination. The incident light field was then limited to the hemisphere above the array. Tominaga et al.[6] calibrated the imaging system using a mirrored ball.

All these works, however, did not intend to infer illumination spectra, but intended to acquire the RGB color distribution of the ambient illumination at a particular point in space. It should be noted that the RGB information of ambient light has very limited applications. For instance, we can create realistic images of natural scenes that are rendered on the spectral information of ambient light, but not on the RGB information.

The present paper proposes a method for estimating an omnidirectional distribution of the scene illuminant spectral power distribution from images taken by a camera aimed at a mirrored ball. We develop a technique for obtaining omnidirectional data more precisely than the previous works, based on calibrated measuring systems. First, we introduce some measuring systems that are designed for acquiring ambient light from any direction at an arbitrary location in a natural scene. Second, we calibrate the measuring systems. A mapping between the coordinates on the image of a spherical ball and the light directions of rays in the world is deter-

[†]Present address: Nagano University, Ueda, Nagano 386–1298, Japan.

Received Jan. 13, 2005; accepted for publication Jun. 16, 2005.
1062-3701/2006/50(3)/217/11/$20.00.

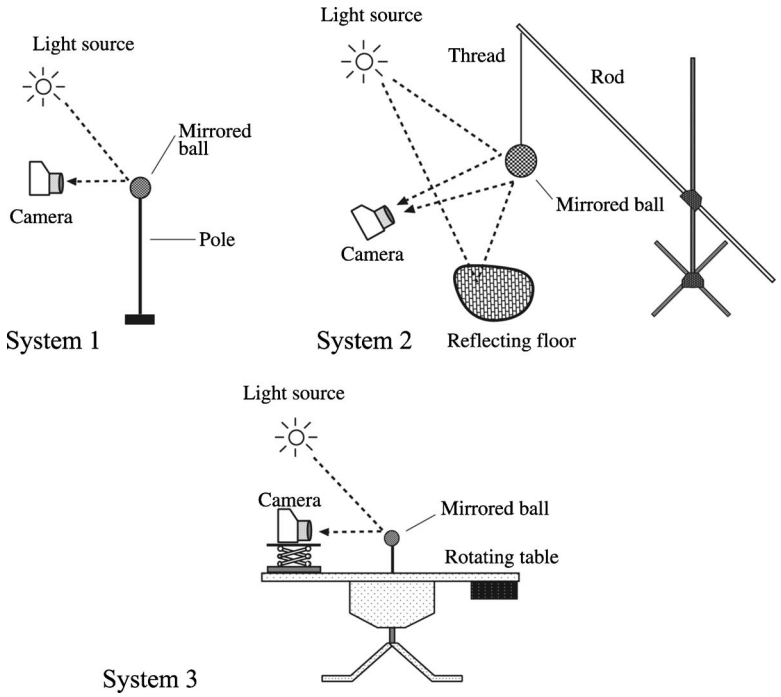

Figure 1. Measuring systems using a mirrored ball.

mined. Then, we create images representing the omnidirectional light distribution. Third, an algorithm is presented for recovering the illuminant spectral-power distribution from the image data of RGB three channels and the calibrated reflectance data of the mirrored ball. Finally, experimental results in a natural environment are shown for demonstrating the feasibility of the proposed method.

MEASURING SYSTEM

Figure 1 shows three types of measuring systems using a mirrored ball that we have built for acquiring ambient light properties at an arbitrary location in a natural scene. System 1 is the most convenient type where a mirrored ball is placed on the top of a thin pole. The ball used in this study is a polished stainless steel ball with a diameter of 5 cm as shown in Fig. 2. Because the camera is separated from the ball, this system can be used at any location in a natural environment. System 2 is a hanging-ball type where the ball is hung on a fish line. This system is useful for collecting light rays from all surroundings by a single ball, including a reflecting floor as a light source. System 3 is the most precise type using a rotating table. The ball is mounted on the top of a short pole about which a table with a length of 80 cm is able to rotate. At the end of the table is a digital camera for imaging a particular view. Because the viewing direction can be rotated arbitrarily in a horizontal plane, multiple images at different viewing angles are combined into an omnidirectional image.

Figure 2. Mirrored ball of polished stainless steel.

One of the advantages of these systems is that the observable range is very wide and the surrounding scenery of the ball for most directions is captured in a single image. Figure 3 shows the real observable range of the present systems. The observable angle is $360° - \psi$, where ψ is the visual angle of the ball. Therefore, the range increases with camera distance from the ball and the decrease of ball size. Note that there always is scene occlusion by the camera itself.

A Canon RGB digital camera, EOS D60, is used for imaging the mirrored ball. Each color channel is represented by 12 bits, and images are sampled on a 2052×3088 pixels lattice. We examined the linearity of the camera response by observing uniform color patches with both the camera and a radiometer. It had a good linearity. Next, we measured the camera sensitivities by using a mono-

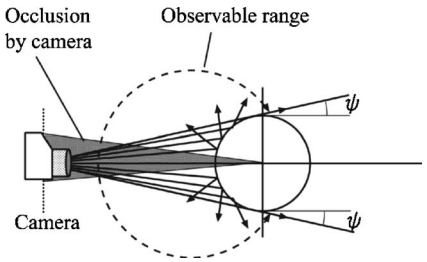

Figure 3. Observable range.

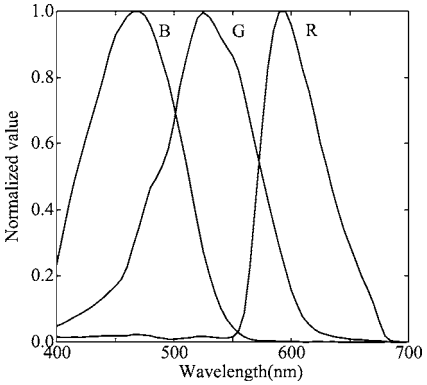

Figure 4. Spectral sensitivity functions of the camera.

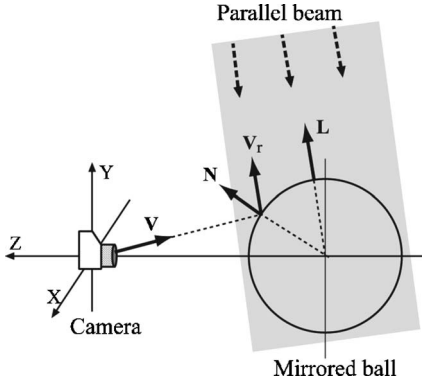

Figure 5. Geometric model for observing a mirrored ball.

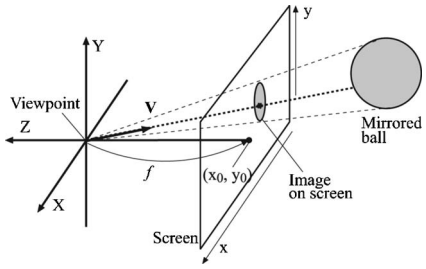

Figure 6. Projection onto an image screen.

chrometer. Figure 4 shows the normalized curves of the spectral sensitivity functions in the tungsten mode. The spectral responses are used for approximating arbitrary illuminant spectra, although the spectral bands are broader than those of a multichannel camera with more than three sensors (e.g., see Ref. 12).

High dynamic range images are captured by the present system. The linearity of the camera response is a nice property for this purpose. We have to capture the full dynamic range of intensities present in a scene. For instance, the direct light sources can be many times brighter than regions in shadow, and thus a single exposure cannot capture both the brightest and darkest details. We used a shutter to extend the dynamic range of the present 12-bit camera. Pictures of the same scene are taken with different shutter speeds (different exposures), and the multiple images are combined into a single image (see Refs. 13 and 14 for the details).

ESTIMATION OF LIGHT DIRECTIONS

Geometric Model

Figure 5 depicts the geometric model for observing a mirrored ball. A camera photographs the spherical mirror to obtain an omnidirectional radiance map around the location where the mirror is placed. In the figure, **N** is the surface normal vector at an observable point on the sphere, **L** is the light direction vector from the spherical center toward the outside, and **V** is the viewing vector from the camera toward the observable point. Moreover, $\mathbf{V}_r$ is the vector obtained by mirroring **V** about **N**. These vectors are represented by three-dimensional column vectors with unit length. We assume that a light source is distant from the ball, and all ray beams originating from the light source are parallel. Therefore, the vector $\mathbf{V}_r$ has the same direction as the light vector **L** from the spherical center.

The light directional vector is described as

$$\mathbf{L} = \mathbf{V}_r = \mathbf{V} - 2(\mathbf{N} \cdot \mathbf{V})\mathbf{N}, \tag{1}$$

where the symbol · denotes the dot product of two vectors.

Camera Calibration

In order to determine precisely the mapping between the image coordinates of the spherical ball and the light directions in the world, we need to know the camera parameters such as the optical axis and the focal length of the optical system. The camera is assumed to be a pinhole camera the image plane of which is composed of a set of rectangular cells of pixels. Figure 6 shows the projection of an object in three-dimensional (3D) space onto a screen by the camera. We call the system of coordinates (X, Y, Z) in the 3D space *the world coordinate system*, and call the system of coordinates (x, y) on the plane *the screen coordinate system*.

The projection equation from the world coordinates to the screen coordinates is described as $\mathbf{P}[XYZ1]^t = s[xy1]^t$, where t stands for matrix transposition and s is a normalization parameter.[15] The projection matrix **P** is defined as

$$\mathbf{P} = \begin{bmatrix} fk_x & 0 & x_0 & 0 \\ 0 & fk_y & y_0 & 0 \\ 0 & 0 & 1 & 0 \end{bmatrix}, \tag{2}$$

where the quantity f represents the focal length, the pair (k_x, k_y) is related to the pixel size, and the coordinates

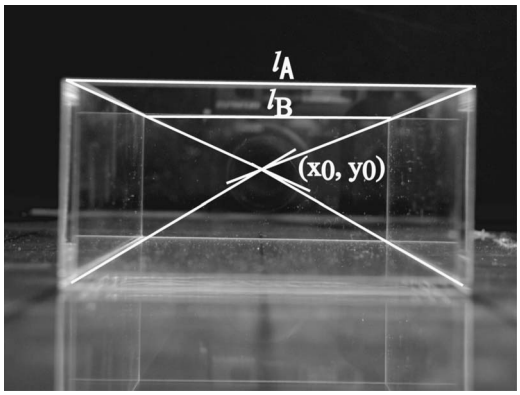

Figure 7. Calibration object for camera parameters.

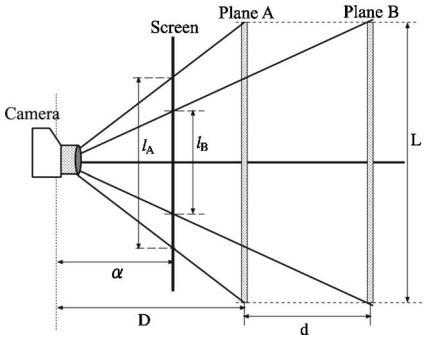

Figure 8. Geometries for camera calibration.

(x_0, y_0) represent the principal point on the optical axis. The focal length is expressed in units of length (say, meters), and (k_x, k_y) is expressed in units of pixel$\times$meter^{-1}. Therefore, the effective focal length is defined as $\alpha_x = fk_x$ and $\alpha_y = fk_y$, which correspond to the size of the focal length in horizontal and vertical pixels, respectively. The quantities (α_x, α_y) and (x_0, y_0) are intrinsic camera parameters that do not depend on the position and orientation of the camera in space.

The world coordinate system (X, Y, Z) is coincident with the camera coordinate system in the sense that the origin is placed at the focal point of the camera, and the Z axis is on the optical axis. Therefore, extrinsic camera parameters are not needed in estimating light-directional vectors. We determine the intrinsic camera parameters according to the following simple and direct procedure. The calibration object we used is a rectangular box made of transparent acrylic resin as shown in Fig. 7.

Figure 8 shows the geometric model of the calibration setup. The box is placed at a distance of D from the camera. Planes A and B are of the same length L at the interval d. Under perspective projection, these two reference objects project their images with different lengths l_A and l_B onto the screen. Then the projection for these objects must satisfy the relations

$$\mathbf{P}[0\ L\ D\ 1]^t = s[0\ l_A\ 1]^t,$$

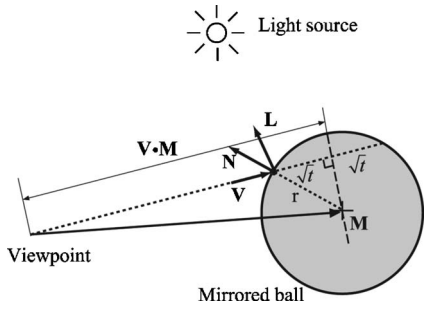

Figure 9. Geometries for computing the surface normal.

$$\mathbf{P}[0\ L\ D+d\ 1]^t = s[0\ l_B\ 1]^t, \tag{3}$$

where $(x_0, y_0) = (0, 0)$ is assumed. Solving these equations leads to $\alpha = l_A l_B d / L(l_A - l_B)$. Thus, the effective focal lengths α_x and α_y are determined, in horizontally and vertically, from the size of the calibration box and the projected lengths. Next, the principal point (x_0, y_0) is determined using the vanishing point. For instance, we use the sidelines combining planes A and B as shown by the diagonal lines in Fig. 7. The vanishing point means the point, which is the image of the common point at infinity of the 3D lines.

Estimation Algorithm

We have to compute the light-directional vector at each pixel point on the mirrored ball. The directional vector **L** is described by Eq. (1), where the viewing vector **V** and the surface normal **N** are unknown. These vectors are calculated using the coordinates of each pixel on the image screen and the camera parameters. Let (x, y) be the coordinates on the image screen, the calculation is performed in two steps.

First, the normalized vector of **V** passing through (x, y) in Fig. 6 is described as

$$\mathbf{V} = \frac{[(x - x_0)/\alpha_x, (y - y_0)/\alpha_y, 1.0]^t}{\|(x - x_0)/\alpha_x, (y - y_0)/\alpha_y, 1.0\|}, \tag{4}$$

where the symbol $\|\cdot\|$ denotes vector length.

Second, the surface normal **N** at the corresponding point of (x, y) on the ball can be determined with the help of Fig. 9, where **M** is the spatial coordinate vector pointing at the ball center, and r is the radius of the ball. We have to examine whether the viewing vector intersects the ball, that is, whether the corresponding point is on the ball or not. The criterion index is defined as

$$t = (\mathbf{V} \cdot \mathbf{M})^2 - (\mathbf{M} \cdot \mathbf{M}) + r^2. \tag{5}$$

The above index is related with the section $\sqrt{t}$ cutoff by **V** as shown in Fig. 9. Therefore, if $t \geq 0$, the viewing vector intersects the ball. Then the distance from the viewpoint to the intersection point is calculated as

$$d_p = \min((\mathbf{V} \cdot \mathbf{M}) - \sqrt{t}, \quad (\mathbf{V} \cdot \mathbf{M}) + \sqrt{t}). \tag{6}$$

Finally, the normal vector **N** can be obtained as

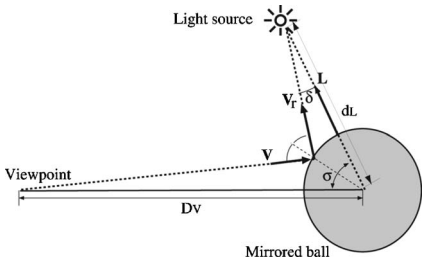

Figure 10. Geometries for observing a light source close to the ball.

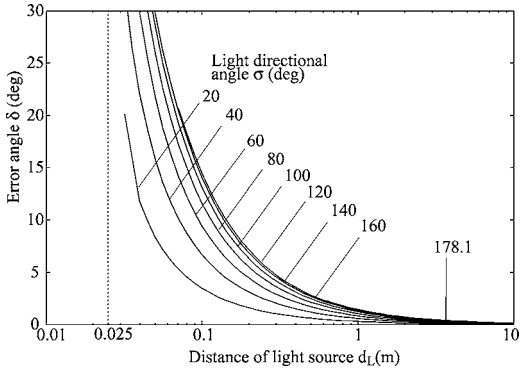

Figure 11. Errors as a function of light source distance with a parameter of directional angle.

$$\mathbf{N} = (d_p\mathbf{V} - \mathbf{M})/\|d_p\mathbf{V} - \mathbf{M}\|. \tag{7}$$

Substituting these **V** and **N** into Eq. (1) completes the calculation of **L**.

Error Analysis

All light sources are assumed to be distant from the mirrored ball. In this case the accuracy of the estimated light direction depends mostly on the reliability of the camera parameters. If the light source is close to the ball, the mirrored vector $\mathbf{V}_r$ is different from the light directional vector. Figure 10 depicts the special case, where the angle δ represents a discrepancy between $\mathbf{V}_r$ and **L**. The error angle depends on the distance d_L and the directional angle σ of a light source. This error angle is also affected by the measurement setup for the ball. Obviously, the error can decrease as the distance D_V to the viewpoint increases and the radius r decreases.

Let us evaluate the error in the case of using system 3 with $D_V = 0.7$ m and $r = 2.5$ cm as shown in Fig. 1. Figure 11 shows the results of numerical calculations for the error angle. The errors are given as a function of the distance d_L with a parameter of the light directional angle σ. The set of the uppermost curves represents an upper limit to the angle error. We have $\delta = 1.43$ deg for $d_L = 1.0$ m and $\delta < 1.0$ deg for $d_L > 1.41$ m. The ball is located at more than 1.5 m above the ground. Thus, we can conclude that the error is less than 1 deg in real scenes.

CREATION OF OMNIDIRECTIONAL IMAGES

Mapping from Ball Images

In order to represent the spatial distribution of ambient lighting, we create an omnidirectional image as a latitude/longitude image in a polar coordinate system. A set of light vectors **L** points in all directions from the spherical center. Therefore, assuming that the viewpoint is located at the spherical center, we can create the omnidirectional image observed at the viewpoint. Let (x_s, y_s, z_s) be the rectangular coordinates for **L** on the spherical ball, where the axis z_s is assumed to be coincident with the optical axis Z, as shown in Fig. 12. The light-directional vector is expressed in the polar coordinates (θ, ϕ) by the transformation

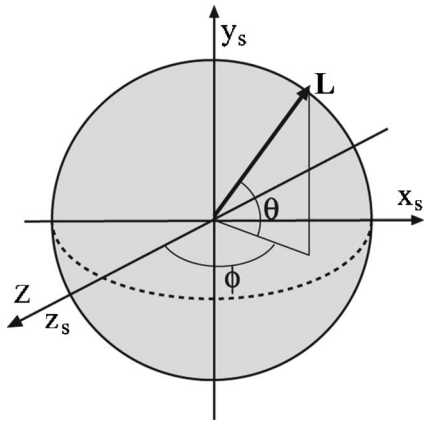

Figure 12. Polar coordinate system.

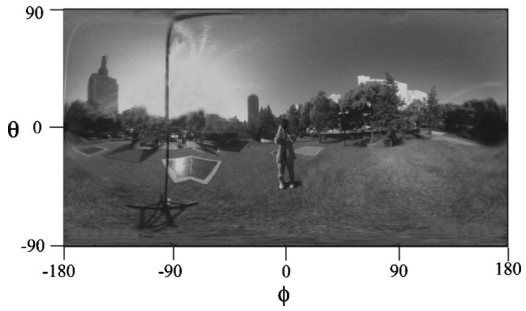

Figure 13. Omnidirectional image in the polar coordinate system.

$$\theta = \tan^{-1}(y_s/\sqrt{x_s^2 + z_s^2}),$$

$$\phi = \tan^{-1}(x_s/z_s). \tag{8}$$

The original image of the mirrored ball is mapped into the plane of (θ, ϕ) based on the knowledge of the light-directional vector at each pixel point. For example, Fig. 2 includes an image of the mirrored ball that was acquired using system 2 in the open air under daylight. The latitude/longitude image from this mirrored-ball image is shown in Fig. 13, it represents the whole surroundings viewed from the ball. Figure 14 shows another omnidirectional representation in polar coordinates, where the bottom figure represents an upper view with the origin at the zenith, and the top figure represents a bottom view with the origin at the nadir.

Image Composition

Let us consider the resolution of the omnidirectional image. The center part of the image corresponding to the spherical

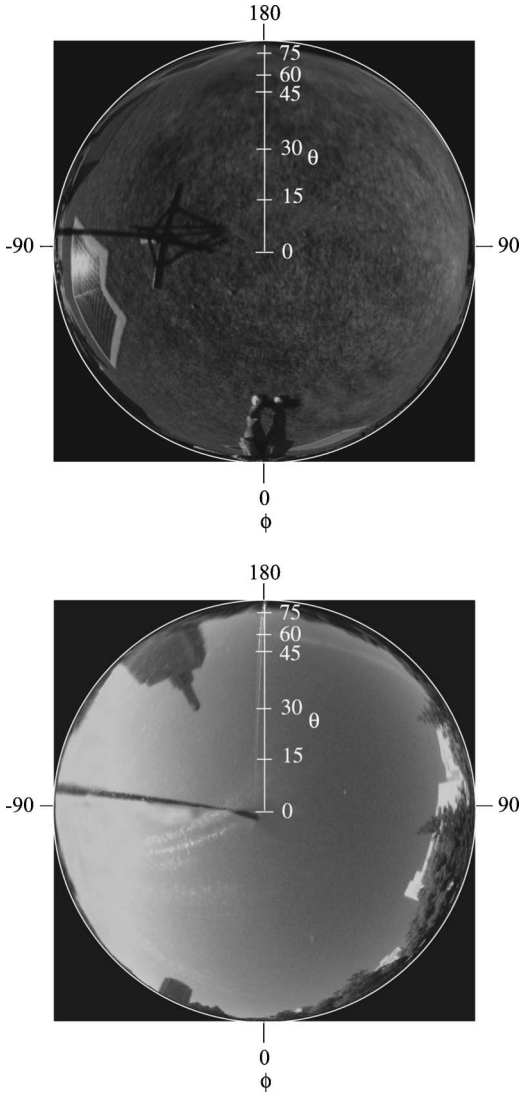

Figure 14. Omnidirectional images of an upper view (bottom) with an origin of the zenith and a lower view (top) with an origin of the nadir.

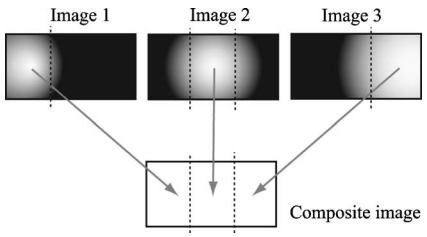

Figure 15. Composition of three images observed in rotation of 120 deg.

center is sampled finely, while the outer part corresponding to the spherical edge is sampled only roughly. In order to eliminate the low resolution, we acquire several images of the ball from different viewing angles, which are combined into one high resolution image. This technique is explained for use of system 3 as follows.

Figure 15 illustrates the composition of three images

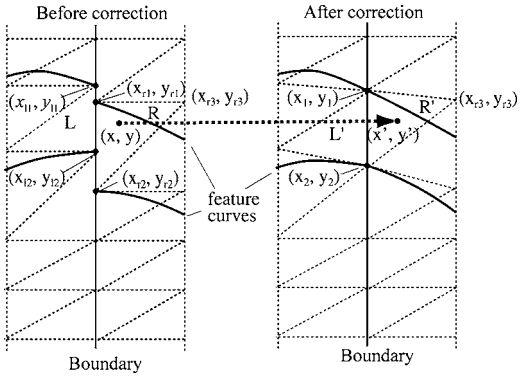

Figure 16. Correction at the boundary for creating a composite image.

observed at rotation angle intervals of 120 deg. Each image of the mirrored ball is transformed into an omnidirectional image in the polar coordinates. Next, a partial image in $[-60° \leqslant \phi \leqslant 60°]$ with high resolution is cut out from the omnidirectional image. Finally, these cutouts are combined into one image.

It should be noted that even small distortions in the original images cause a discrepancy between two images and makes the image composition complicated. The left of Fig. 16 depicts the boundary area when two partial images are put side by side. The two curves have gaps at the boundary between the left and right images. These gaps cause a discrepancy in color. We propose a correction algorithm for creating a combined image without such discrepancies. Clear curves, object edges, and color boundaries in the observed images are extracted as feature curves of the original scene. Then the left and right images are deformed so that all feature curves meet smoothly without gaps at the boundary area. This image correction can be devised based on an *affine transformation*.[15]

Our algorithm consists of three steps:

(1) Left and right images are decomposed into triangular patches, where the end point of each feature curve is assigned to the vertex of a triangle as shown on the left of Fig. 16.

(2) Let $(x_{\mathrm{l}i}, y_{\mathrm{l}i})$ and $(x_{\mathrm{r}i}, y_{\mathrm{r}i})$ $(i=1,2,3)$ be the vertices of the triangles L and R, respectively. The meeting points of the feature curves are determined at the boundary as

$$x_i = \frac{x_{li} + x_{\mathrm{R}i}}{2},$$

$$y_i = \frac{y_{li} + y_{\mathrm{R}i}}{2},$$

$$i = 1,2. \tag{9}$$

(3) The triangles L and R are deformed into L' and R' as shown on the right of Fig. 16. The inner point

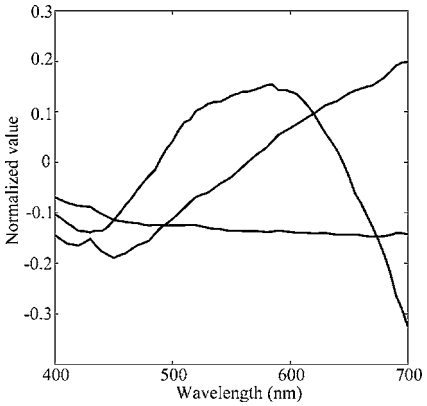

Figure 17. Basis functions for illuminant spectra.

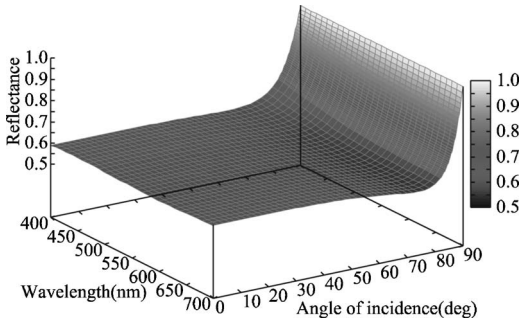

Figure 18. Computed spectral reflectance for the stainless steel as a function of wavelength and incidence angle.

(x,y) is then transformed into (x',y') to keep the linear combination of the two vectors from the fixed vertex (x_{r3},y_{r3}). This condition is described as

$$\begin{bmatrix} x-x_{r3} \\ y-y_{r3} \end{bmatrix} = w_1 \begin{bmatrix} x_{r1}-x_{r3} \\ y_{r1}-y_{r3} \end{bmatrix} + w_2 \begin{bmatrix} x_{r2}-x_{r3} \\ y_{r2}-y_{r3} \end{bmatrix}, \tag{10}$$

$$\begin{bmatrix} x'-x_{r3} \\ y'-y_{r3} \end{bmatrix} = w_1 \begin{bmatrix} x_1-x_{r3} \\ y_1-y_{r3} \end{bmatrix} + w_2 \begin{bmatrix} x_2-x_{r3} \\ y_2-y_{r3} \end{bmatrix}. \tag{11}$$

The weighting coefficients w_1 and w_2 for any point (x,y) are calculated from simultaneous equations in (10), and the new coordinates (x',y') are determined from (11) with the calculated values of w_1 and w_2. The earlier transformation is reduced to a type of the affine transformation.

Finally, we cannot escape from the scene occlusion by the camera itself as shown in Fig. 3. The occluded area is recovered from the corresponding area in the other images taken with different viewing angles. Debevec provided a tool for this correction.[16]

Figure 19. Real view of system 3 in the gym.

ESTIMATION OF ILLUMINANT SPECTRA

Illuminant Recovery from Camera Data

A finite dimensional linear model is used to describe the spectral functions of illuminants. This model is effective in the sense that spectral functions with continuous spectra are represented by only a small number of basis functions. Judd et al.[17] analyzed the measured spectra of daylight at different times of days, under different weather conditions, and on different continents. They showed that daylight spectra were represented by a mean spectral curve and two basis curves. Tominaga[12] introduced a method for choosing the appropriate dimension of the linear model and showed that the dimension was approximately three in his system for a set of spectra from such sources as daylights and an incandescent lamp. As a result, the linear model with three parameters makes it possible to recover the spectral functions from the RGB camera data.

We assume that the illuminant spectrum $E(\mathbf{L},\lambda)$ in a direction $\mathbf{L}$ from the mirrored ball can be expressed as a linear combination of three basis functions as

$$E(\mathbf{L},\lambda) = \varepsilon_1(\mathbf{L})E_1(\lambda) + \varepsilon_2(\mathbf{L})E_2(\lambda) + \varepsilon_3(\mathbf{L})E_3(\lambda), \tag{12}$$

where $\{E_i(\lambda),\ i=1,2,3\}$ is a statistically determined set of basis functions, and $\{\varepsilon_i(\mathbf{L})\}$ is a set of weighting coefficients. To derive the illuminant basis functions, we used a set of measured spectra from the CIE standard lights and several real sources.[13] Figure 17 shows the basis functions used in this study, which were obtained as the first three principal components of the set of illuminant spectra.

The camera output from location x on the mirrored ball is described as

$$\begin{bmatrix} R(x) \\ G(x) \\ B(x) \end{bmatrix} = \int_{400}^{700} S(x,\lambda)E(\mathbf{L},\lambda) \begin{bmatrix} r(\lambda) \\ g(\lambda) \\ b(\lambda) \end{bmatrix} d\lambda, \tag{13}$$

where $S(x,\lambda)$ is the surface-spectral reflectance function of the mirrored ball, and $\{r(\lambda),\ g(\lambda),\ b(\lambda)\}$ are the spectral sensitivity functions of the camera. We consider the illuminant estimation in the visible range of 400–700 nm because of the camera sensitivities. Therefore the limits of integration in Eq. (13) are selected as 400–700. The camera data at

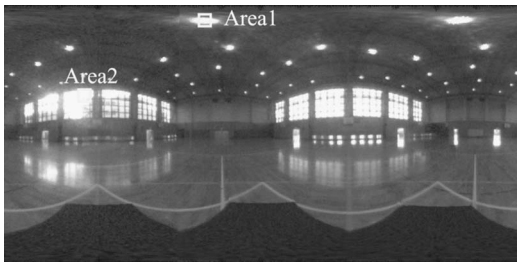

Figure 20. Omnidirectional image of the gym.

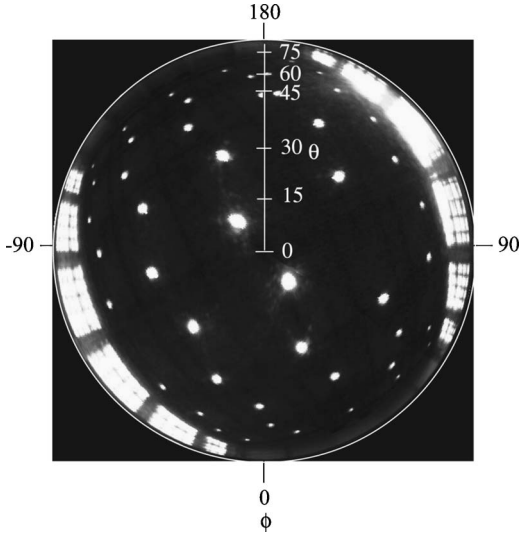

Figure 21. Upper viewing image of the gym.

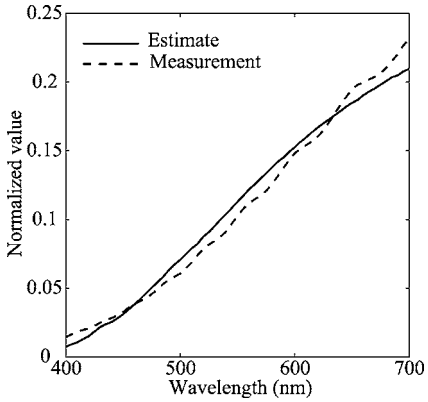

Figure 22. Estimation results of illuminant spectra for a ceiling lamp.

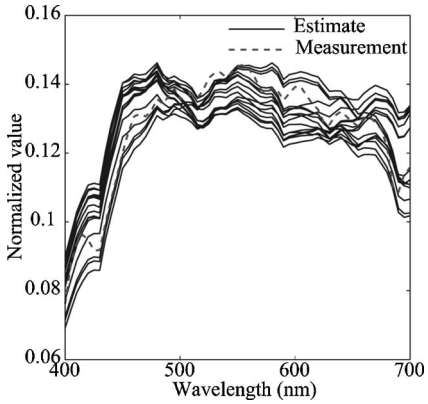

Figure 23. Estimation results of illuminant spectra for lights through a side window.

any location x on the mirrored ball are related to the direction $\mathbf{L}$ via the omnidirectional image. The illuminant weight vector $\boldsymbol{\varepsilon}(\mathbf{L})=[\varepsilon_1(\mathbf{L}),\varepsilon_2(\mathbf{L}),\varepsilon_3(\mathbf{L})]^t$ is estimated from the RGB camera values in the form

$$\boldsymbol{\varepsilon}(\mathbf{L}) = \boldsymbol{\Lambda}_S^{-1}\boldsymbol{\rho}(x), \tag{14}$$

where $\boldsymbol{\rho}(x)$ is the camera output vector defined by $\boldsymbol{\rho}(x)=[R(x),G(x),B(x)]^t$ and $\boldsymbol{\Lambda}_s^{-1}$ is a 3×3 inverse matrix of $\boldsymbol{\Lambda}_s$ with such elements as $\int E_i(\lambda)S(x,\lambda)r(\lambda)d\lambda$, $\int E_i(\lambda)S(x,\lambda)g(\lambda)d\lambda$, and $\int E_i(\lambda)S(x,\lambda)b(\lambda)d\lambda$ $(i=1,2,3)$. Finally, the estimated curve of the illuminant $E(\mathbf{L},\lambda)$ is obtained by substituting the estimate of $\boldsymbol{\varepsilon}(\mathbf{L})$ into Eq. (12).

Reflectance Computation of the Mirrored Ball

The polished metal is an isotropic homogeneous material, and the reflectance function of the specular surface is described by the Fresnel reflectance[18]

$$S(x,\lambda) = F[\theta_i,n(\lambda),k(\lambda)], \tag{15}$$

where θ_i is the angle of incidence to the surface, $k(\lambda)$ is the absorption coefficient, and $n(\lambda)$ is the index of refraction. The angle of incidence is calculated as $\theta_i=\cos^{-1}(\mathbf{N}\cdot\mathbf{L})$. The mirrored ball used in this paper is made from stainless steel (SUS304). The SUS304 steel is an alloy of iron (74%), chrome (18%), and nickel (8%). Generally, the reflectance of a segregation alloy is described as a weighted mean of the contained materials. Consequently, the spectral reflectance $S(x,\lambda)$ can be described as a function of the incident angle of illumination as follows:

$$S(x,\lambda) = 0.74F[\theta_i,n_{F_e}(\lambda),k_{F_e}(\lambda)] + 0.18F[\theta_i,n_{C_r}(\lambda),k_{C_r}(\lambda)] + 0.08F[\theta_i,n_{N_i}(\lambda),k_{N_i}(\lambda)]. \tag{16}$$

The optical constants $[n_{F_e}(\lambda), k_{F_e}(\lambda)]$, $[n_{C_r}(\lambda), k_{C_r}(\lambda)]$, and $[n_{N_i}(\lambda), k_{N_i}(\lambda)]$ are the refractive indices and absorption coefficients for iron, chrome, and nickel, respectively.

We use the database by Callet[19] for the numerical values of these optical constants. If unpolarized light is incident, the Fresnel reflectance is

$$F[\theta_i,n(\lambda),k(\lambda)] = \frac{1}{2}\{R_\perp[\theta_i,n(\lambda),k(\lambda)] + R_\parallel[\theta_i,n(\lambda),k(\lambda)]\}, \tag{17}$$

where $R_\perp$ is the component polarized perpendicular to the plane of incidence and $R_\parallel$ is the component polarized parallel to the plane of incidence. The following Fresnel equa-

tions for calculating the two components were derived by many authors:

$$R_{\perp}[\theta_i, n(\lambda), k(\lambda)] = \frac{a^2 + b^2 - 2a\cos(\theta_i) + \cos^2(\theta_i)}{a^2 + b^2 + 2a\cos(\theta_i) + \cos^2(\theta_i)}, \tag{18}$$

$$R_{\parallel}[\theta_i, n(\lambda), k(\lambda)] = R_{\perp}[\theta_i, n(\lambda), k(\lambda)] \times \frac{a^2 + b^2 - 2a\sin(\theta_i)\tan(\theta_i) + \sin^2(\theta_i)\tan^2(\theta_i)}{a^2 + b^2 + 2a\sin(\theta_i)\tan(\theta_i) + \sin^2(\theta_i)\tan^2(\theta_i)}, \tag{19}$$

where

$$a = \sqrt{\frac{1}{2}}\sqrt{\sqrt{[n^2(\lambda) - k^2(\lambda) - \sin^2(\theta_i)]^2 + 4n^2(\lambda)k^2(\lambda)} + [n^2(\lambda) - k^2(\lambda) - \sin^2(\theta_i)]^2}, \tag{20}$$

$$b = \sqrt{\frac{1}{2}}\sqrt{\sqrt{[n^2(\lambda) - k^2(\lambda) - \sin^2(\theta_i)]^2 + 4n^2(\lambda)k^2(\lambda)} - [n^2(\lambda) - k^2(\lambda) - \sin^2(\theta_i)]^2}. \tag{21}$$

Figure 18 shows the calculated spectral reflectance for the stainless steel as a function of wavelength and the angle of incidence. It should be noted that the reflectance increases abruptly as the angle of incidence approaches the grazing angle of over 75 deg.

EXPERIMENTAL RESULTS

Fist of all, the intrinsic camera parameters were estimated by measuring the calibration box. The effective focal lengths and the principal point are $(\alpha_x, \alpha_y) = (12\,343, 12\,225)$ and $(x_0, y_0) = (1588, 1030)$ in pixel units, respectively. Omnidirectional scene illuminants were acquired in our university gymnasium. Figure 19 shows the real view of system 3 used in this experiment. The indoor scene contains direct illuminations from ceiling lamps and daylights through windows, and indirect illuminations from the surrounding object sur-

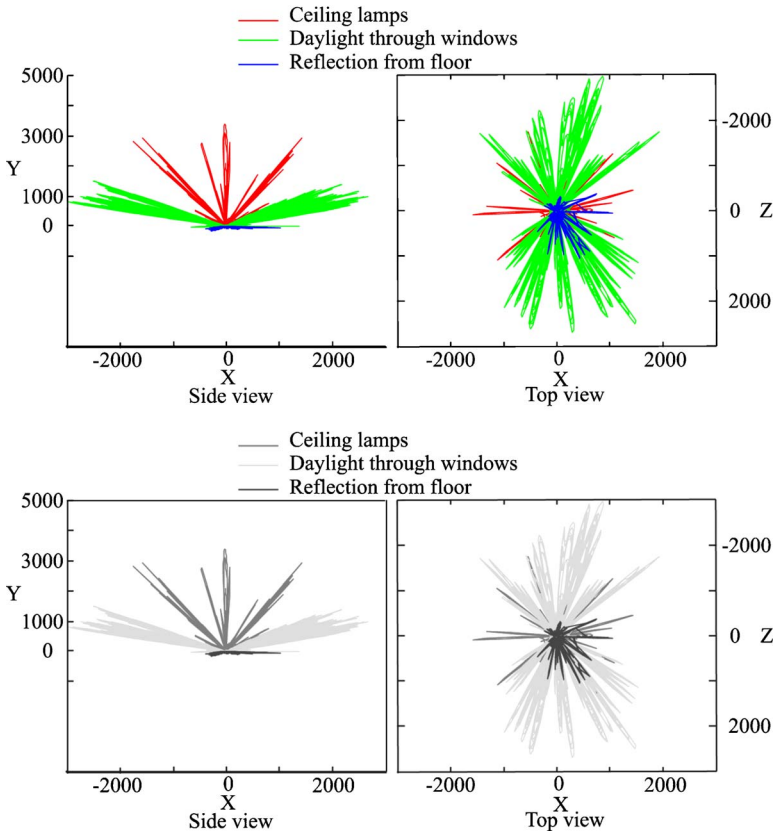

Figure 24. Directional distribution of illuminant power in side view (left) and top view (right). (Available in Color as Supplemental Material on the IS&T website, www.imaging.org.)

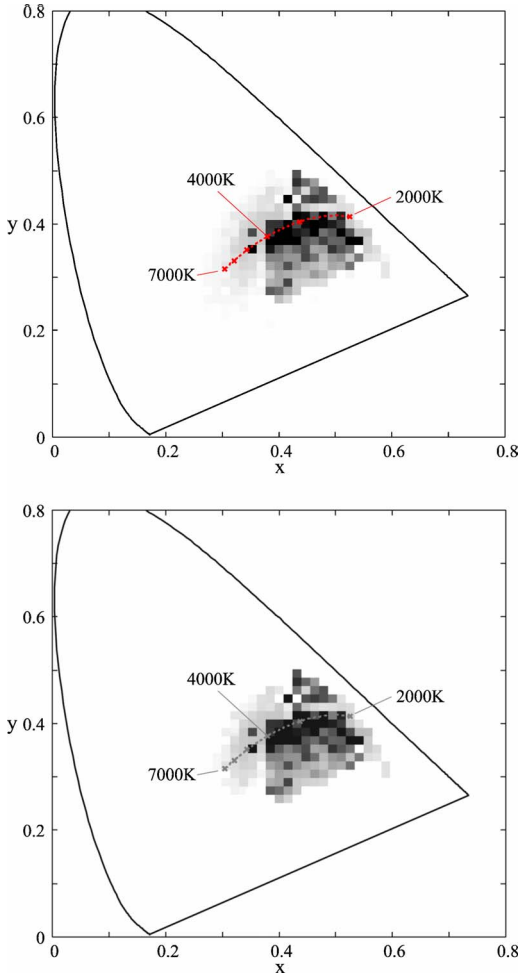

Figure 25. Illuminant chromaticity distribution on the CIE-*xy* diagram. (Available in Color as Supplemental Material on the IS&T website, www.imaging.org.)

faces. The image intensities vary greatly on pixels. The brightest pixels belong to the daylight.

Next, three images of the same scene were taken with the camera at three shutter speeds, and then the images were combined into a high dynamic range image with 14 bits. Second, three high dynamic range images were combined in three directions which are separated 120 deg. Finally, these images were transformed into polar coordinates and the partial images in the $[-60° \leq \phi \leq 60°]$ range were combined into a single 14-bit omnidirectional image. Figure 20 shows the resultant latitude/longitude image, where the black area in the lower part corresponds to the rotating table. We note that the line running across the omnidirectional image corresponds to the circle in the original scene in Fig. 19. These properties suggest the geometrical accuracy of the omnidirectional image. Figure 21 shows the top view image of the gym, which includes a regular array of ceiling lamps and window frames. The main light sources of the gym are ceiling lamps and the windows.

We sampled each spectral power distribution at 61 equally spaced wavelength points throughout the visible region of 400–700 nm. The 61-dimensional vector of this illuminant spectrum was then estimated from the camera data at each pixel point of the omnidirectional image. For example, Fig. 22 shows the estimation results of illuminant spectra for area 1 in Fig. 20, which corresponds to a ceiling lamp. The bold curve indicates the estimated spectrum of the incandescent light source, and the broken curve is the direct measurement by using a spectroradiometer. Figure 23 shows the estimation results for area 2, corresponding to the light source through a side window. The estimated spectral curves have some variations at different pixel points. The comparisons between the estimates and measurements suggest the reliability of the proposed illuminant estimation method.

Moreover, Fig. 24 (available in color as Supplemental Material on the IS&T website www.imaging.org) shows the directional distribution of illuminant power in the separation of the top view and the side view, where the power is depicted as the length of the 61-dimensional illuminant vector, and the origin $(X,Y,Z)=(0,0,0)$ is the center of the ball. The light sources are classified into the three groups of the ceiling lamps, the daylights through side windows, and the reflected lights from the floors, which are painted in red, green, and blue in the figure. Figure 25 (available in color as Supplemental Material on the IS&T website www.imaging.org) shows the chromaticity histogram of the omnidirectional illuminants on the CIE-*xy* diagram. The number of illuminants with the same chromaticity is represented as gray levels. The gradation from black to white means a decrease in the number of illuminants with the same chromaticity. The broken curve indicates the locus of the blackbody radiator. The light sources in the gym are very varied and the chromaticites are widely distributed.

It should be noted that all these results on omnidirectional scene illuminants can be obtained by simply using an off-the-shelf RGB digital camera and a mirrored ball.

CONCLUSION

This paper has proposed a method for estimating the omnidirectional distribution of the scene illuminant spectral-power distribution from images taken by a camera aimed at a mirrored ball. We have developed a technique for precisely obtaining omnidirectional data. First, the measuring systems using a color camera and a mirrored ball were shown for acquiring ambient light at any location in natural scenes. Second, in order to estimate the direction from which light reaches the ball, we calibrated the measuring systems and determined a mapping between the image coordinates of the spherical ball and the light directions of rays in the world. Then, an omnidirectional image representing the spatial distribution of ambient light sources was created in a polar coordinate system. Third, an algorithm was presented for recovering the illuminant spectral-power distribution from the RGB data at the respective pixel points and the surface reflectance data of the mirrored ball. Finally, an experiment was executed in a gymnasium with multiple light sources. The results demonstrate that reliable omnidirectional illuminant spectra can be estimated by the proposed method.

ACKNOWLEDGMENTS

The authors thank Professor Brian Wandell for useful discussions on this study.

REFERENCES

[1] S. Tominaga and B. A. Wandell, "Natural scene illuminant estimation using the sensor correlation", Proc. IEEE **90**(1), 42–56 (2002).
[2] P. M. Hubel, "The perception of color at dawn and dusk", *Proc. IS&T/SID Seventh Color Imaging Conference: Color Science, Systems, and Applications* (IS&T, Springfield, VA, 1999) pp. 48–51.
[3] J. Hong, X. Tan, B. Pinette, R. Weiss, and E. M. Riseman, "Image-based homing", IEEE Control Syst. **12**(1), 38–45 (1992).
[4] P. E. Debevec, "Rendering synthetic objects into real scenes", *Proc. SIGGRAPH 98*, 1998, pp. 189–198.
[5] J. Unger, A. Wenger, T. Hawkins, A. Gardner, and P. E. Debevec, "Capturing and rendering with incident light fields", *14th Eurographics Workshop on Rendering* (Eurographics Association, Aire-la-Ville, Switzerland, 2003), pp. 141–149.
[6] S. Tominaga and N. Tanaka, "Measurement of omnidirectional light distribution by a mirrored ball", *Proc. IS&T/SID Ninth Color Imaging Conference* (IS&T, Springfield, VA, 2001) pp 22–26.
[7] K. Miyamoto, "Fish eye lens", J. Opt. Soc. Am. **54**(8), 1060–1061 (1964).
[8] I. Sato, Y. Sato, and K. Ikeuchi, "Acquiring a radiance distribution to superimpose virtual objects onto a real scene", IEEE Trans. Vis. Comput. Graph. **5**(1), 1–12 (1999).
[9] K. Yamazawa, Y. Yagi, and M. Yachida, "Omnidirectional imaging with hyperboloidal projection", *Proceedings of the International Conference Intelligent Robotics and Systems* (IEEE, New York, 1993), pp. 1029–1034.
[10] S. K. Nayar, "Catadioptric omnidirectional camera", *Proceedings of the 1997 Conference Computer Vision and Pattern Recognition* (IEEE, New York, 1997), pp. 482–488.
[11] For example, see http://www.debevec.org.
[12] S. Tominaga, "Spectral imaging by a multi-channel camera", J. Electron. Imaging **8**(4), 332–341 (1999).
[13] S. Tominaga, "Multichannel vision system for estimating surface and illumination functions", J. Opt. Soc. Am. A **13**(11), 2163–2173 (1996).
[14] P. E. Debevec and J. Malik, "Recovering high dynamic range radiance maps from photographs", *Proc. SIGGRAPH 97*, 1997, pp. 369–378.
[15] O. Faugeras, *Three-Dimensional Computer Vision* (The MIT Press, Cambridge, MA, 1999).
[16] http://www.ict.usc.edu/graphics/HDRShop/.
[17] D. B. Judd, D. L. MacAdam, and G. W. Wyszecki, "Spectral distribution of typical daylight as a function of correlated color temperature," J. Opt. Soc. Am. **54**, 1031–1040 (1964).
[18] M. Born and E. Wolf, *Principles of Optics* (Pergamon, Oxford, 1987), pp. 36–51.
[19] http://virtual.pl.ecp.fr/~callet/.